nature photonics

SUPPLEMENTARY INFORMATION

https://doi.org/10.1038/s41566-019-0360-3

In the format provided by the authors and unedited.

Programmable plasmonic phase modulation of free-space wavefronts at gigahertz rates

Alexei Smolyaninov*, Abdelkrim El Amili, Felipe Vallini, Steve Pappert and Yeshaiahu Fainman

Department of Electrical & Computer Engineering, University of California, La Jolla, CA, USA. *e-mail: asmolyan@eng.ucsd.edu

Programmable Plasmonic Phase Modulation of Free-Space Wavefronts at GHz Rates

Alexei Smolyaninov, Abdelkrim El Amili, Felipe Vallini[1], Steve Pappert, and Yeshaiahu Fainman

Supplementary Materials

Contents

Section S1 – Conceptual Illustration 2

Section S2 – Polarization Contrast Imaging 5

Section S3 – Spatial Light Modulation State of the Art 7

Section S4 – Plasmonic Cross Talk and a Full Model of the SPR Resonances 8

Section S5 – Electrical Cross-Talk 10

Section S6 – Electrical Bandwidth and Wavelength Acceptance 11

Section S7 – Additional Topics 13

S7a. Film Stability 13

S7b. Ag Film Thickness and Degradation 13

S7c. Noise and relative intensity of pixels in Polarization Contrast Imaging 13

S7d. Noise in MZI Measurements 13

S7e. Potential Applications 14

S7f. Advances in Electro-Optic Thin Films via Electric Field Induced Second Harmonic Generation 15

References 17

Section S1 – Conceptual Illustration

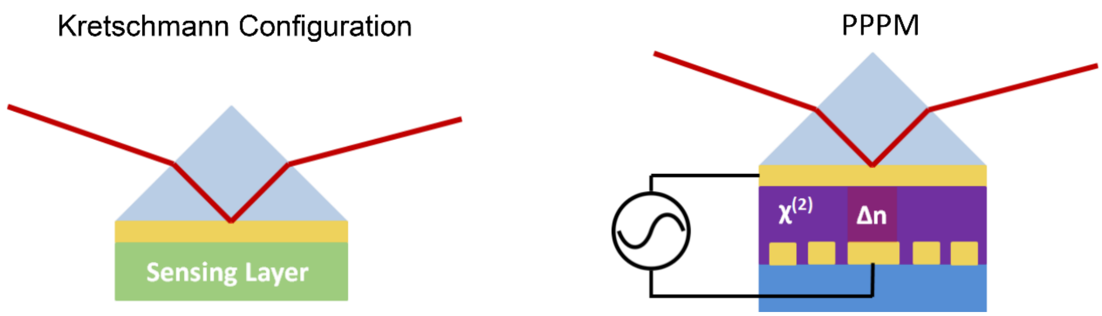

Fig S1. Simplified illustration of the operating principle of the PPPM

Let us consider the traditional Kretschmann configuration (Fig S1): a three layer system consisting of a dielectric prism, a noble metal thin film, and another dielectric - the sensing layer - with light incident on the metal thin film at or near the surface plasmon angle θ_{sp} given by the phase matching condition: $k_{sp} = k_0\sqrt{\varepsilon_m\varepsilon_d/(\varepsilon_m + \varepsilon_d)}$ and $k_{sp} = k_x = k_0\sqrt{\varepsilon_{prism}}sin\theta_{sp}$. Here, k_{sp} is the surface plasmon wave vector, k_0 is the free space wave vector, k_x is the plane parallel component of k_0, while ε_m, ε_d, and ε_{prism} are the complex permittivity's of the thin noble metal. dielectric layer, and prism respectively [29-31]. The Fresnel reflection coefficients for this three-layer system are given by:

$$r = \frac{r_{01} + r_{12}exp(2ik_{1z}d)}{1 + r_{01}r_{12}exp(2ik_{1z}d)} \qquad (eq. 2)$$

Where, $r_{ij} = \frac{Z_i - Z_j}{Z_i + Z_j}$, $Z_i = \frac{\varepsilon_i}{k_{iz}}$ for p polarization and $Z_i = k_{iz}$ for s polarization, $k_{iz} = k_0(\varepsilon_i - \varepsilon_0 sin^2\theta)^{1/2}$. Here θ is the angle of incidence, d is the thin metal thickness, and the indices i, j correspond to the prism (i, j = 0), the metal layer (i, j = 1), or the sensing layer (i, j = 2) [29-31]. The intensity reflectance due to spr is then given by $R = |r|^2$ and the phase shift on reflection ϕ is given by solving $r = |r|exp(j\phi)$ for $\phi = Arg(r)$[31]. It should be noted that only p polarized light, not s polarized light is subject to SPR. This is expressed here analytically in the Fresnel reflection coefficients via the discrepancy in Z_i terms for p and s polarizations. Under SPR conditions

$r_p \neq r_s$ and $\phi_p \neq \phi_s$; this effect allows for SPR-based polarimetry, ellipsometry, and phase-contrast imaging [14, 19-22, 32]. R_p and ϕ_p are extremely sensitive to any changes in refractive index ($\Delta n \approx \sqrt{\Delta\varepsilon_i}$), film thickness ($d$), or the angle of incidence (θ). In the PPPM (Fig S1) described in this paper, the sensing layer is replaced with a modulation layer consisting of a dielectric whose refractive index is modulated via the linear electro-optic (EO) or pockel's effect to exploit this sensitivity, with additional possible third order $\chi^{(3)}$ contributions to the electro-optic effect (e.g. the quadratic electro optic effect) as discussed in section S7f and detailed at length in refs [28, s5].

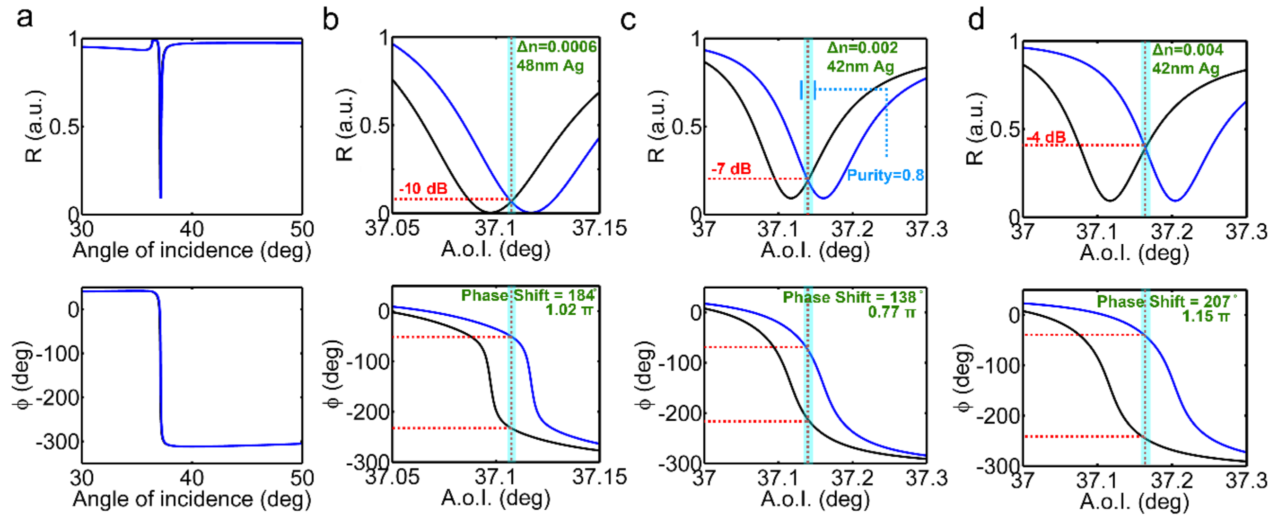

Fig S2. Reflectivity and phase shifts due to SPR as a function of incident angle for a SI prism with an Ag SPR film and AlN modulation layer for varying thickness of Ag films and refractive index modulation (Δn). The black curves represent the unmodulated phase and intensity response of the system with an AlN refractive index of n=2.1176 as a function of angle of incidence. The blue curves represent the phase and intensity of the reflected light as a function of incident angle with the refractive index of the AlN layer shifted to n+Δn. Insertion loss at the bias point for modulation is indicated in red on the reflectivity curves. The bias point is (a) Overview of the SPR reflectivity and phase shift over a wide angular range (b) SPR characteristics near θ_{sp} of 48 nm Ag film with Δn=0.0006. (c) SPR characteristics near θ_{sp} of 42 nm Ag film with Δn=0.002. (d) SPR characteristics near θ_{sp} of 42 nm Ag film with Δn=0.004.

Several example characteristic curves of SPR induced reflectivity and phase shift calculated from the above Fresnel equations and SPR phase matching condition are shown in Fig S2. The angular bandwidth of the PPPM is determined by the desired modulation purity, in our case $p = 0.8$. Purity in this reflective phase-dominant modulator can be defined as $p = \Delta\phi_p/\Delta R_p$. Angular bandwidth, then, is the range of angles of incidence θ about a given bias point θ_b that satisfy our purity requirements. The bias point occurs near θ_{sp} and is specified as the intersection of two R_{sp} curves separated by some Δn that modifies the refractive index in the permittivity ε_2 term ($\varepsilon_2 = n_2^2 - k_2^2$) in the modulation layer of the three-layer Fresnel equations given above. The bias point likewise sets the theoretical insertion loss for the PPPM. The material of the selection prism is also important; in order to satisfy the SPR phase matching condition, the refractive index of the prism must be greater than that of the sensing layer. [29-31]. Consequently, if one wishes to use higher index dielectrics as a modulation layer in the Kretschmann configuration, one must use higher index prisms as well. The dielectrics used in this work (AlN and

SRN) have n≈2.1. This, combined with transparency at telecom wavelengths, made Si the obvious choice for the prism material. The optical path necessary for SPR excitation at the calculated θ_{sp} (Fig S2) is illustrated in Fig S3

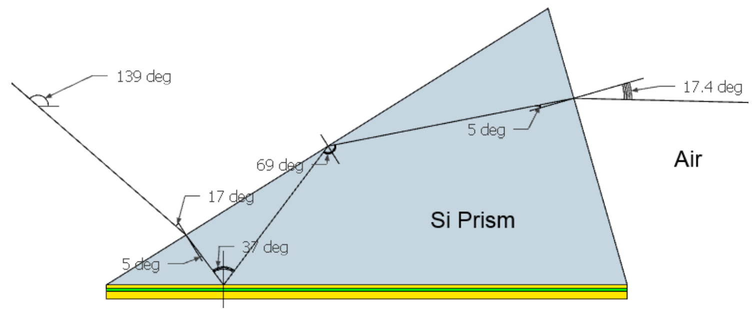

Fig S2. Illustration of the optical path taken in the modulator.

For applications of high speed spatial light modulation using an SPR-based approach, four coupled design characteristics matter: extinction ratio, purity, angular bandwidth, and insertion loss. To illustrate these design constraints, three sets of R_p and ϕ_p curves of particular Si Prism-Ag-AlN systems are shown as a function of angle of incidence and electrically induced Δn in Fig S2 b-d. Given an electro-optic Δn, potential phase modulation due to SPR can be determined analytically by taking the intersection of the SPR reflectivity curves as the angular bias point for phase modulation and evaluating the corresponding phase shift (Fig S2). The ability for a single pixel of the modulator to achieve at least a π phase shift is desirable for a PPPM. Extinction ratio can increase by either increasing Δn or narrowing the SPR resonance via adjusting metal film thickness and thereby increasing the slope of the ϕ_p curves via a kramers-kronig relation at the cost of increased insertion loss and reduced angular bandwidth. When possible, increasing Δn is obviously preferable. For a given material, increasing Δn requires increasing the electric field and therefore voltage applied to the $\chi^{(2)}$ material; such an approach is limited by the breakdown characteristics of the material in question. As an example, for a Si Prism and a 48 nm Ag SPR film with a 100 nm AlN modulation layer, one needs a $\Delta n = 0.0006$ applied to the modulation layer to realize a ~π phase shift in the reflected p-polarized light (Fig S2 b). From eq. 1, we see that AlN (r_{33} = 1pm/V, n=2.1176), requires an applied field of 143 MV/m which is below the reported breakdown field for AlN of 210 MV/m [33]. To apply the required 143 MV/m field (E=V/d), a potential (V-π) of 14V is applied to the gold electrodes that form the space variant modulation matrix of the PPPM. Invariably, imperfections in the fabrication process will affect these characteristics. Surface roughness of the electro optic thin film on the sapphire wafer hosting the electrode matrix will degrade modulation performance by potentially increasing the distance between the electrodes and the SPR thin film thereby decreasing the applied electric field and by introducing air gaps which may increase the distance between the SPR thin film and the modulation layer.

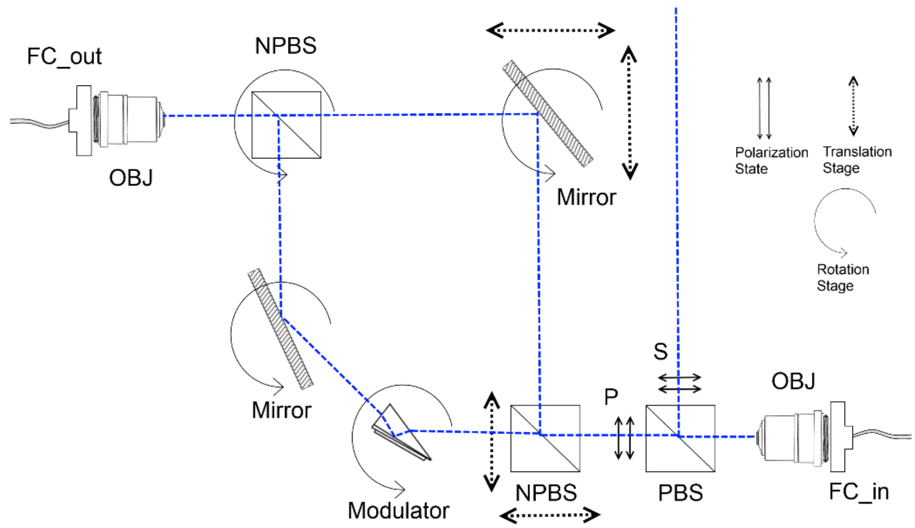

Fig S4. Schematic of the MZI Measurement System

Section S2 – Polarization Contrast Imaging

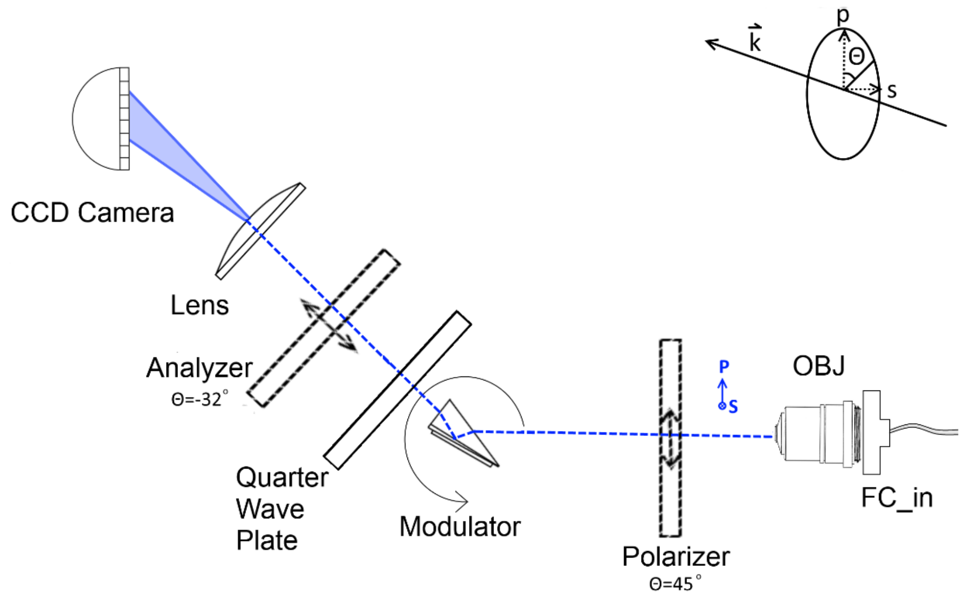

Fig S5. Schematic of the Polarization Contrast Imaging Setup.

Analytically, the intensity of the reflected light can be written in terms of the two orthogonally polarized waves

$I = E_p^2 \cos^2(\Theta) + E_s^2 \sin^2(\Theta) + E_p E_s \sin(2\Theta)\cos(\phi_p)$ where E_p and E_s are the amplitudes of the reflected p and s polarized waves respectively, Θ is the angle of the analyzer relative to the polarizer(Fig S5), and ϕ_p is the phase shift induced in the p-polarized wave during reflection under SPR conditions [21]. Using this self-referencing technique, the SPR induced phase shift in the reflected beam can be experimentally characterized by studying the intensity of light as a function of analyzer angle. We are interested in detecting a space-variant phase shift of ϕ_p, so instead we perform a polarization contrast imaging measurement at a single Θ that produces maximum intensity contrast between PPPM pixels in the 'on' and 'off' state. An electro-optically induced shift in R_p will adjust the relative phase of the co-linear fields $\overrightarrow{E_p}$ and $\overrightarrow{E_s}$ thereby varying the polarization state of the reflected field. This change in polarization state can be detected through the intensity of the light after it passes through an analyzer. The intensity contrast between the two modulation states, 'on' and 'off', is maximized at $\Theta = \psi + \frac{\pi}{2} + \sqrt{\arctan(1 - e^2)}$ [19]. Where ψ is the angle of the major axis of the polarization ellipse of the superposition of $\overrightarrow{E_p} + \overrightarrow{E_s}$ and e is the eccentricity of that polarization ellipse. For our experimental system, this occurred at $\Theta \approx -32.1^o$.

Section S3 – Spatial Light Modulation State of the Art

Table S1. Per pixel characteristics of state of the art spatial light Modulation schemes.

	Modulation Bandwidth (kHz)	Insertion Loss (dB)	Driving power (mW per pixel)	V-π; Driving Voltage to achieve π phase shift per pixel (V per pixel)	Pixel Size (μm^2)
Commercial DMD [1]	**40 kHz**	**0.5 dB**	**0.0002 mW**	N/A	**187 μm^2**
Ferroelectric Liquid Crystal [2]	**10 kHz**	**2.2 dB**	Unspecified	**0.005 V**	**174 μm^2**
High Voltage MEMS DMD [3]	**500 kHz**	**0.2 dB**	Unspecified	**50 V**	**1600 μm^2**
PPPM (this work)	**1,000,000 kHz (1 GHz)**	**10 dB**	**120 mW**	**18 V**	**3025 μm^2**

Table S1 provides a brief overview of some state of the art works spatial light modulation. The Programmable Plasmonic Phase Modulator (PPPM) in this work is intended as a first demonstration of ultra-high speed 2D control of free-space optical fields. Works [1]-[3] consist of arrays on the order of ~800 x ~1200. The presented PPPM is only a 4x4 demonstration of the plasmonic-linear electro-optic transduction mechanism for space variant modulation. As discussed in the manuscript, the active layer of the PPPM had an r_{33} of at most 1 pm/V. Currently, integrated plasmonic modulators operating at GHz frequencies have been demonstrated using nonlinear chromophores with r_{33} values in excess of 100 pm/V [9-10]. Using such polymers could reduce power consumption to the order of ~1 mW per pixel while retaining GHz modulation bandwidth. When combined with through-silicon vias for high density integration [36], this presents a path for the realization of ultra-high speed plasmonic SLMs. Note that pixel size for the PPPM takes into account inter-pixel separation to mitigate plasmonic cross talk (see section S4).

Section S4 – Plasmonic Cross Talk and a Full Model of the SPR Resonances

Our device consists of 30 μm x 45 μm pixels with an inter-pixel separation of 55 μm (Figure 4). The theoretical decay length of an SPP propagating along a metal film is given by:

$$L = \frac{1}{2k_x^{"}}$$

Where the wave vector of the SPP propagating along the surface is given by

$$k_x = k_x' + ik_x^{"} = \left[\frac{\omega}{c}\left(\frac{\varepsilon_1'\varepsilon_2}{\varepsilon_1' + \varepsilon_2}\right)^{1/2}\right] + i\left[\frac{\omega}{c}\left(\frac{\varepsilon_1'\varepsilon_2}{\varepsilon_1' + \varepsilon_2}\right)^{3/2}\frac{\varepsilon_1^{"}}{2(\varepsilon_1')^2}\right]$$

Where the permittivity of the metal is given by $\varepsilon_1 = \varepsilon_1' + i\varepsilon_1''$ and the permittivity of the dielectric is ε_2.

The decay length of the SPP may then be re-written as:

$$L = \frac{1}{2\left[\frac{2\pi}{\lambda}\left(\frac{\varepsilon_1'\varepsilon_2}{\varepsilon_1' + \varepsilon_2}\right)^{3/2}\frac{\varepsilon_1^{"}}{2(\varepsilon_1')^2}\right]}$$

For the device used in our manuscript, λ=1.55 μm, From silver: ε_1'=-129.17, ε_1''=3.28 (Johnson & Christy), and for Aluminum Nitride ε_2= 4.48. Using these values produces a theoretical decay length (1/*e*) of L=125 μm.

However, this is for a simplified model of our system. The simplified 3 layer model provided of our device neglects the gold contacts which fall well within the decay width of the plasmon. The decay width of the plasmon may be estimated by:

$$z_d = \frac{\lambda}{2\pi}\sqrt{\frac{|\varepsilon_1'| + \varepsilon_2}{\varepsilon_2^2}}$$

Using the above values, we find a decay width (as defined by the 1/*e* point) of the Si-Ag-NL plasmon to be z_d=1.27 μm. The dielectric layer used for electro-optic modulation in our device has thicknesses ranging from 93 nm to 200 nm, depending on the device; therefore, plasmons beneath our electrical contacts will be subject to losses induced by the full 50 nm Au layer which at λ=1550nm has a permittivity of $\varepsilon_{1(Au)} = \varepsilon_1' + i\varepsilon_1''$= -115.13 + i * 11.259. It is useful to note that the losses, as characterized by the complex permittivity, induced by the 50nm Au layer are notably higher than those of the 48 nm Ag layer: $\varepsilon_1''_{(Au)}$= 11.259 > $\varepsilon1''_{(Ag)}$= 3.28. Re-calculating the decay length to include this added loss provides a decay length of L = 28 μm which is notably smaller than the inter-pixel separation of 55 μm. Additionally, it should be noted that the above are theoretical calculations which assume perfectly uniform thin films. In practice, surface roughness from thermal and RF sputtered thin films, such as the ones used in this manuscript, further reduces the propagation length due to scattering losses. This is quantified analytically and experimentally in [11, s1-s2] and would reduce the propagation length and therefore plasmonic cross talk further beyond what is calculated here.

Since we have considered the effect of the Au layer, it may be useful to fully model all layers of our device. We consider the full structure of our device, that is: Si (bulk) - Ag (48nm) - EO Dielectric (93nm-200nm) - Au (50nm) - Air (bulk).

To solve for the reflectivity and phase of a five layer system we solve for the Fresnel coefficients recursively. For three layers i, j, k, the Fresnel coefficient are given by a generalized form of eq.2 form the supplementary materials:

$$r_{ik} = \frac{r_{ij} + r_{jk} exp(2ik_{jk}d)}{1 + r_{ij}r_{jk} exp(2ik_{jk}d)}$$

For a five layer system, the terms r_{01}, r_{12}, r_{23}, r_{34} are computed. Then the full system may be solved recursively for r_{24}, r_{14}, and the full system r_{04}, i.e:

$$r_{24} = \frac{r_{23} + r_{34} exp(2ik_{34}d)}{1 + r_{23}r_{34} exp(2ik_{34}d)}$$

$$r_{14} = \frac{r_{12} + r_{24} exp(2ik_{24}d)}{1 + r_{12}r_{24} exp(2ik_{24}d)}$$

$$r_{04} = \frac{r_{01} + r_{14} exp(2ik_{14}d)}{1 + r_{01}r_{14} exp(2ik_{14}d)}$$

The procedure for solving each of these terms, as well as extracting the corresponding reflectivity and phase shift is detailed in supplementary section s1.

For the materials and device used in this manuscript, over the angular range of interest (37^{o} specifically and more broadly the 30^{o}-50^{o} range, as illustrated in Figure S2), solving for the full five layer system amounts to a minor correction in reflected intensity and phase shift. This is illustrated in supplementary Figure s6.

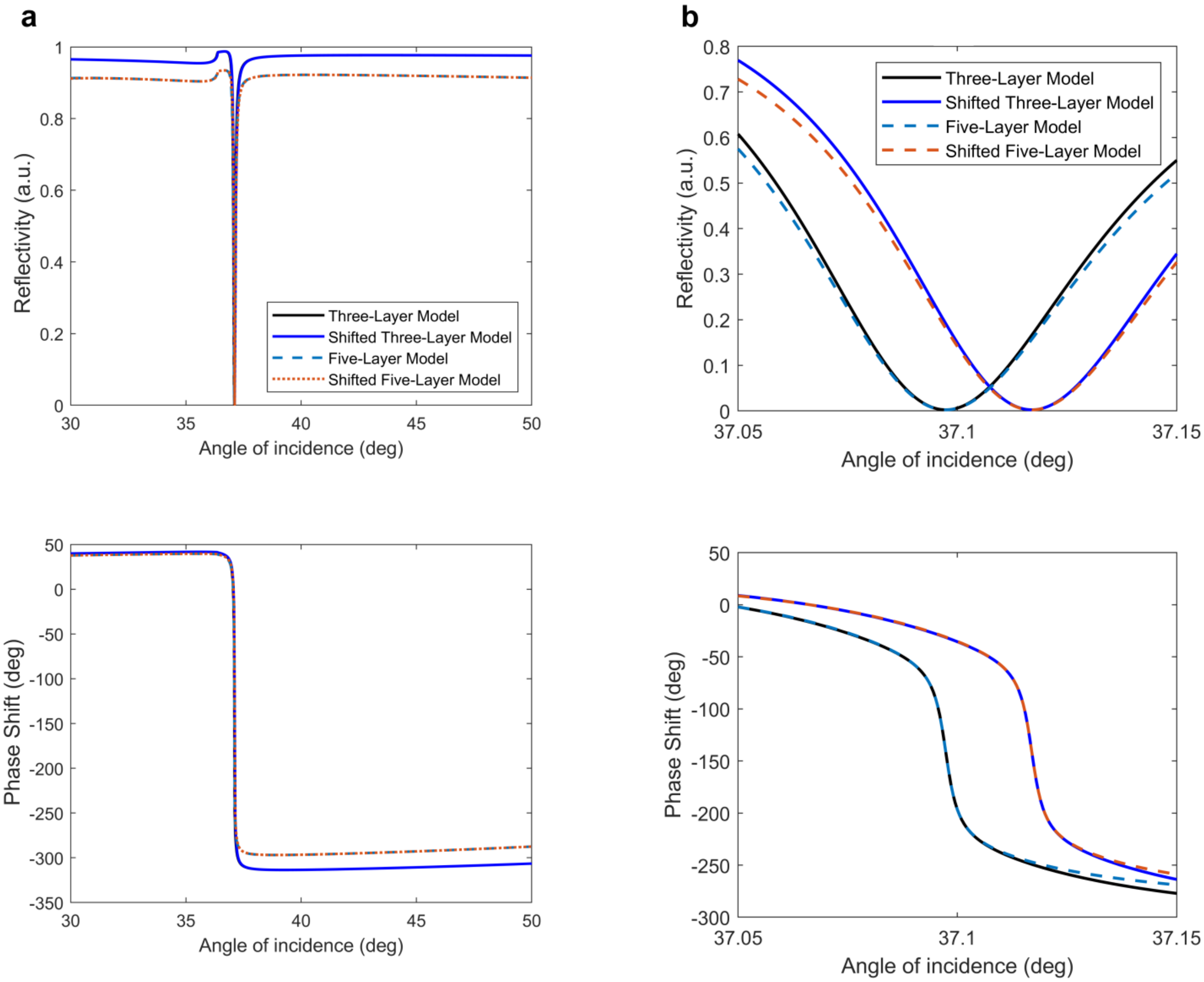

Fig S6. Comparison of Three-Layer SPR Resonance Model to Five-Layer SPR Resonance Model over the angular range of interest

Section S5 – Electrical Cross-Talk

The inter-pixel separation of our device is 55 µm. At their closest, some wires (Figure 4) may come within 25 µm of a differently addressed pixel. The gap between Au contacts and the Ag SPR film is at most 200 nm. Assuming both are perfect parallel plate capacitors and can be approximated by $E \approx V/d$, the worst case scenario of fringing electric fields is well over two orders of magnitude lower than the driving field (V/25,000 nm vs. V/200 nm). For cross-talk between pixels directly, the worst-case estimate is even lower (V/50,000 nm vs. V/200 nm). Furthermore, the height of the metal contacts is only 50 nm, the minimum width of the metal contacts is 35,000 nm, therefore the parallel plate capacitor estimation above is a far better approximation of the driving field and is an overestimation of the fringing fields. Even assuming both are perfect parallel plate capacitors, cross talk due to fringing electric fields between pixels is necessarily less than 1% simply due to the dimensionality involved.

Intuitively, this makes sense given the vast array of electrically driven CMOS and silicon-photonics devices that have sub 10μm spacing between electrical wires, pins, through-silicon VIAs and other contacts.

Section S6 – Electrical Bandwidth and Wavelength Acceptance

If we consider the wavelength acceptance to be defined as the spectral bandwidth i.e. the spectral range over which the device operates above the -3dB point relative to its center wavelength (1550 nm in our case), then the PPPM is simply limited by the transmission window of silicon in the near-infrared which for the case of a bulk Si prism, we take to be 1200 nm onwards. We have provided characteristic curves of theoretical performance at wavelengths of 1200 nm, 1550 nm, and 1800 nm. Moreover, there is some variation as to which angle satisfies the phase matching condition for the system, as illustrated by the characteristic curves in our response; however, this can be satisfied by simply rotating the prism. Additionally, the bandwidth of the phase shift and corresponding modulation purity are shown in S7c-d.

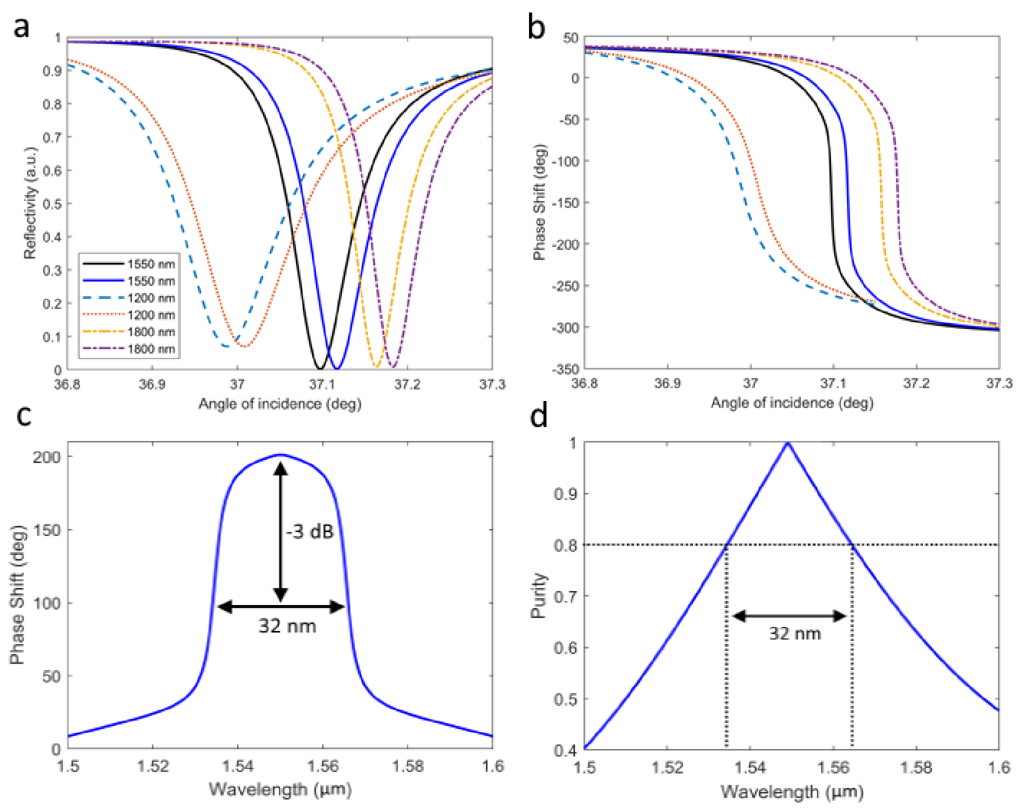

Fig S7. a-b.Characteristic Curves for the SPR resonance of the device at wavelengths of 1200 nm, 1550nm, and 1800nm illustrating operation over the near infrared transmission window of silicon. c. theoretical phase shifting as a function of wavelength for the reported AlN device. d. theoretical modulation purity, defined by the relative change in reflected intensity as we move away from the selected bias point of the device when operating across the 32nm spectral range in (c).

Figure S7c shows theoretical phase shifting as a function of wavelength for the reported AlN device. Using the industry standard -3db definition, our device has a spectral bandwidth of operation of 32nm operating at a center frequency of 1550nm. Additionally, Figure S7d illustrates the theoretical modulation purity, defined by the relative change in reflected intensity as we move away from the selected bias point of the device when operating across that 32nm spectral range. Modulation purity over this range is 80% or greater. The decreased sensitivity to shifts in wavelength as compared to shifts in angle or refractive index is consistent with literature that reports wavelength interrogation of SPR being up to two orders of magnitude less sensitive then angular interrogation and phase interrogation SPR. [21, S16]

In the MZI measurement setup, the operational bandwidth of our device was limited by the electrical bandwidth of the probes used to drive the modulator. Figure S8 below illustrates this bandwidth.

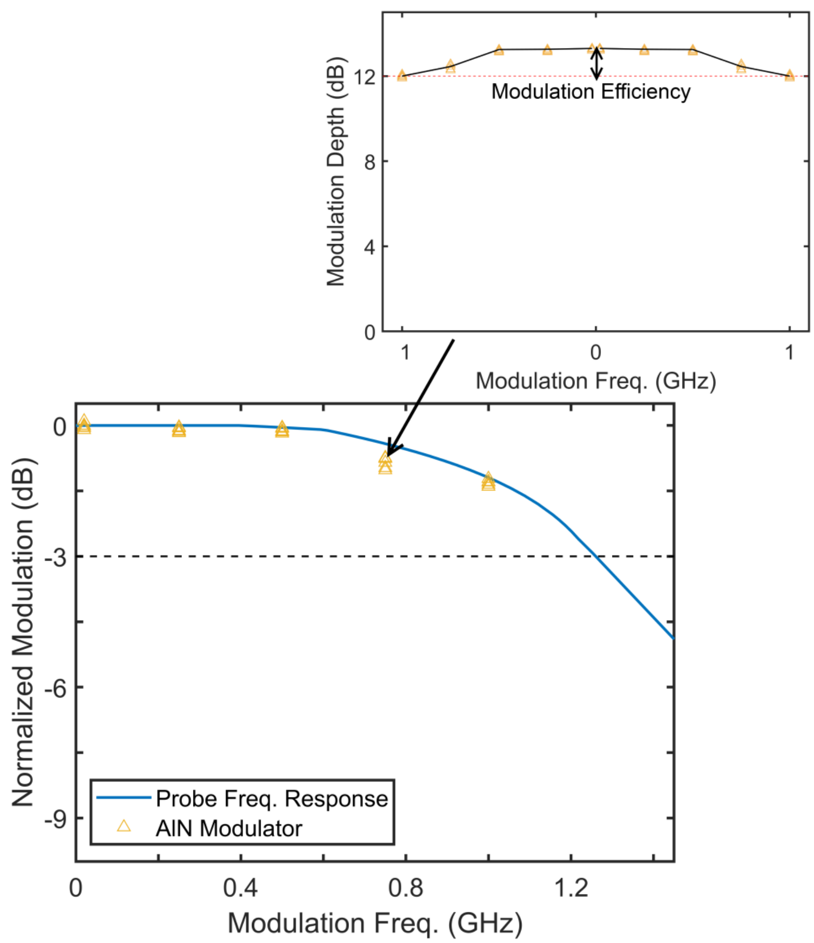

Fig S8. Normalized modulation as a function of the modulation frequency at small signal operation. There is no indication for a bandwidth limitation beyond that of the probe used to drive the PPPM up to 1 GHz at a wavelength of 1550nm Inset: The modulation efficiency is the ratio between the maximum extinction ratio measured in the MZI setup at a modulation frequency of 20 kHz and the extinction ratio measured at other modulation frequencies.

Section S7 – Additional Topics

S7a. Film Stability

The EO performance is reproducible from Film to Film assuming similar deposition parameters (e.g. same gas ratios for SRN deposition via PECVD). The Aluminum Nitride in this paper reproduces the AlN film in [33]. The electro optic performance of SRN in this manuscript is consistent with that of reported SRN values (r_{33}=0.2-0.3pm/V) in literature [s3,s4] for a 500 sccm Silene PECVD process[s5]. Both Aluminum Nitride and SRN are thermally stable well above 350k. [33,s6-s8]

S7b. Ag Film Thickness and Degradation

The film thickness (48nm) was verified using a Daktak 150 Surface Profiler which has a manufacturer specified maximum vertical resolution of 1Å over a vertical range of 6.55µm over a transvers scan length of 55mm. We estimate a surface roughness of 4 Å in the e-beam evaporated Ag layer.

With regards to Ag degradation, as calculated in the added supplementary section S4, the decay width of the Silicion-Ag plasmon, as defined by its 1/*e* point, extends for 1.27 µm; so were a surface oxide in air where to form, the Si-Ag plasmon would still "see" the shift in from the electro-optic layer. It is most likely that any surface oxidation on the Ag-electro-optic interface would manifest as a small shift in the coupling angle for optimum phase matching for each wavelength of operation and possibly small reduction of the electric field across the nonlinear material layer.

S7c. Noise and relative intensity of pixels in Polarization Contrast Imaging

The relative intensity of the pixels is consistent from image to image e.g. the brightest pixels in the 's' in fig 4e are consistent in terms of relative intensity with the brightest pixels in the middle two column of figure 4b which has all pixels active. In general, the pixels have some degree of non-uniformity due to some non-uniformity in the fabrication of the multilayer thin-film structure. These non-uniformities are visible in fig 4a. More sophisticated electrode patterning techniques, such as the vertical contacts (VIAs) used in CMOS processes may alleviate these defects while allowing much larger pixel arrays to be driven. Additionally these are free-space optical measurements; especially under quasi DC conditions, such as those in the polarization contrast imaging setup, some variance from image to image is expected due to factors such as mechanical instability.

S7d. Noise in MZI Measurements

Noise source contributions for the measurement include noise from the laser source and thermal noise in the EO converter used for detection. In order to illustrate this, we have provided a trace of an unmodulated signal passing through our MZI in Figure S9

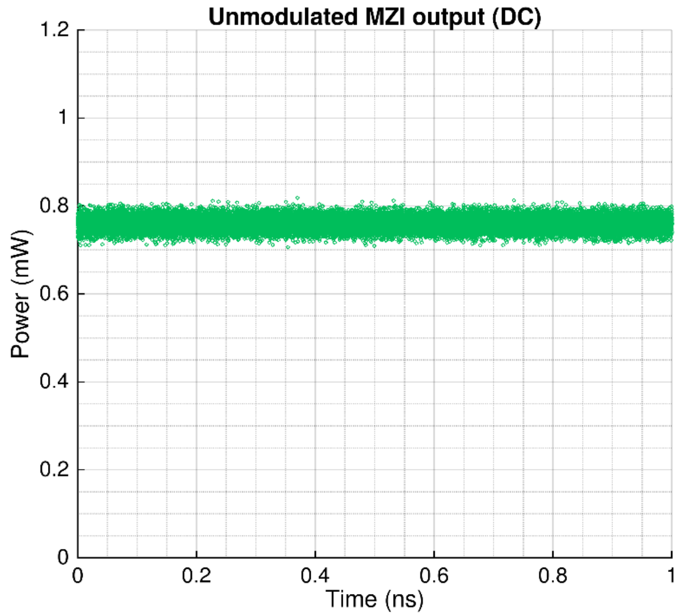

Fig S9. Unomodulated signal illustrating laser source and thermal noise in the MZI illustrate din Figure 2b.

By a significant margin, the primary noise source in the measurement comes from the Erbium-Doped Fiber Amplifier (EDFA), which had a measured noise figure (NF) of 5.6 dB. An EDFA was used to drive up the input optical power during characterization of the reported device in order to mitigate the reported ~10 dB insertion loss of the device which is discussed at length in supplementary sections S1 and S3, and illustrated in supplementary figure S2 and table S1, and is discussed in the main manuscript as well as the methods. Potential solutions that would reduce this insertion loss are mentioned in the main text of the manuscript as well as in greater detail in supplementary sections S1, S3, S7c, and S7f.

S7e. Potential Applications

One of the more common commercial spatial light modulation technologies, liquid crystal polarization grating (LCPGs) often utilize only a π phase shift in a quarter-waveplate, half-waveplate, quarter-waveplate (QHQ) scheme first investigated by Pancharatnam [r9] where a change in the polarization azimuth angle β between a half wave plate, quarter wave plate sandwich produces a phase shift of 2β [s10].

Indeed, the same polarization rotation principal used in a QHQ setup (e.g. Figure 12 in [s10]) has also been used to improve contrast in polarization contrast imaging setups [17-20] and is very similar to the polarization contrast imaging used in this manuscript (Figure 2 B, Figure S 5) to evaluate the space variant phase shift (Figure 4), which operates on the same principal: rotating polarization azimuths in between birefringent media to achieve a phase shift; in our case we achieve this by using the PPPM to impart an additional phase delay onto the TM component of light relative to the TE and then imaging through a λ/4 plate. In principal, however, the PPPM described in this manuscript is fully compatible with a QHQ setup which would allow us to achieve phase shifts of 2.2π in polarization contrast mode.

Additionally, the reported ~π phase shift of the PPPM is sufficient to realize two-level binary phase control of light at GHz rates, which has potential applications such as discrete step beam steering [36-38].

S7f. Advances in Electro-Optic Thin Films via Electric Field Induced Second Harmonic Generation

In this initial demonstration of SPR enhanced $\chi^{(2)}$ nonlinearities in a solid state medium for high speed free-space electro-optic transduction, an spr thin film was selected with a narrow resonance to work in conjunction with existing linear electro-optic thin films (SRN, AlN). Currently, as grown dielectric thin films of SRN have an r_{33} of 0.2-0.3 pm/V [s3,s4]. However, cutting-edge developments in electric field induced second harmonic generation (EFISH) in certain materials such as SRN (used in this manuscript) have provided a new avenue for a high effective $\chi^{(2)}$. Using EFISH and a quasi-DC bias field applied across the thin film to induce a high effective $\chi^{(2)}$ via the material's $\chi^{(3)}$ nonlinearity, these cutting edge developments have realized coefficients as high as 22pm/V[s5], almost two orders of magnitude greater than previously reported values.

The current manuscript does not utilize an EFISH induced $\chi^{(2)}$ in SRN; however, as the EFISH work has only recently been published [s17]. Extrapolating these cutting edge developments to the presented work, we show that if a coefficient of 22 pm/V in SRN is achieved, then a resonance that is several orders of magnitude broader may be utilized with corresponding gains in angular bandwidth, phase modulation, and purity as illustrated below in figure S10. Figure S10 models the same PPPM presented in this manuscript, but utilizing an EFISH induced nonlinearity in SRN as opposed to utilizing Pockel's effect directly. The cyan window in (a) illustrates the significantly greater acceptable angular bandwidth (0.3°, significantly greater than the divergence of a collimated laser beam), purity, and phase shift as compared to Fig S2.

Additionally, figure S11 illustrates theoretical performance curves for the same films used in this manuscript (SRN) under EFISH conditions (electric-field induced second harmonic generation) with nonlinear coefficients in the 8 pm/V and 22 pm/V range reported in preprint [s17] and compares them with theoretical curves for 1 pm/V films used in the reported PPPM. Supplementary figure S11 illustrates the theoretical wider acceptance of the device using EFISH materials. Furthermore, SRN under EFISH is not the only solid-state integratable platform that can achieve a high electro-optic coefficient. Recently, much work has been done with Lithium-Niobate on Silicon, which has an even greater r_{33} >30 pm/V [39-40, s18], which allows for further improved performance.

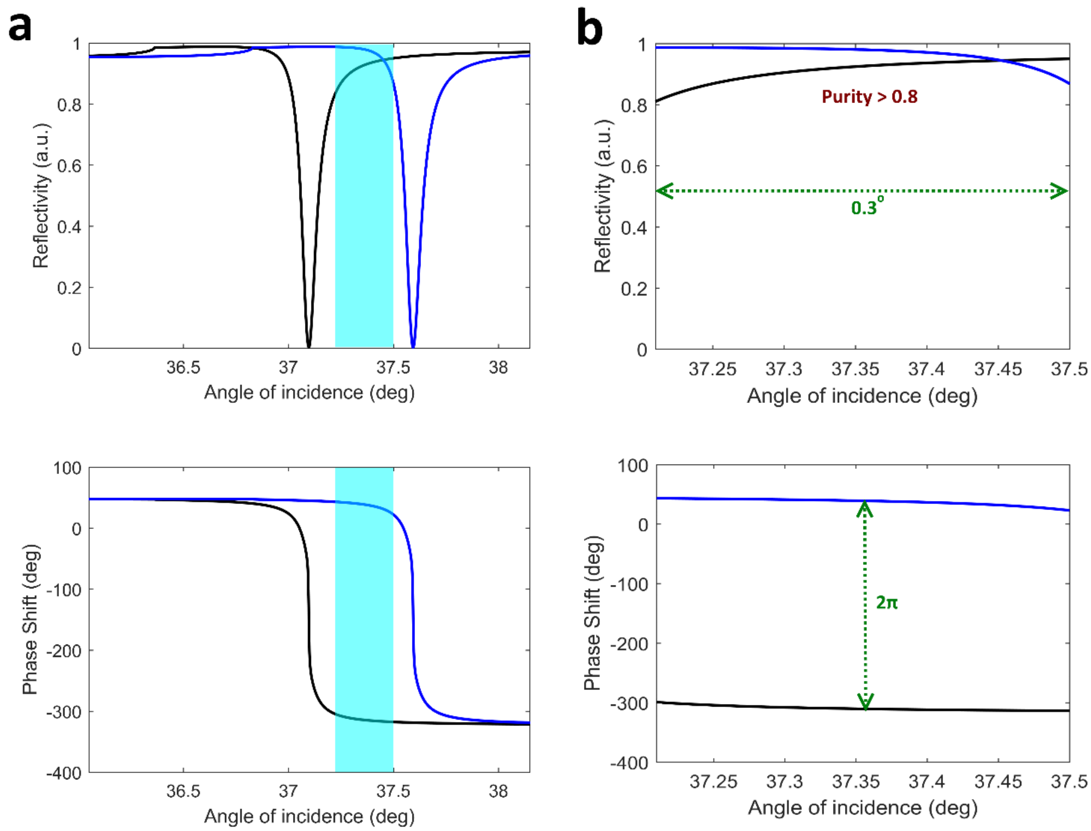

Fig S10. Theoretical reflectivity and phase shifts due to SPR as a function of incident angle for a SI prism with a 48nm Ag SPR film and an EFISH SRN modulation layer (93nm) with an EO coefficient of 22 pm/V as reported in [s17] The black curves represent the unmodulated phase and intensity response of the system with an EFISH SRN thin film as a function of angle of incidence. The blue curves represent the phase and intensity of the reflected light as a function of incident angle with the refractive index of the SRN layer shifted via the EFISH effect. (a) Overview of the SPR reflectivity and phase shift over a wide angular range (b) SPR characteristics near θsp of 48 nm Ag film.

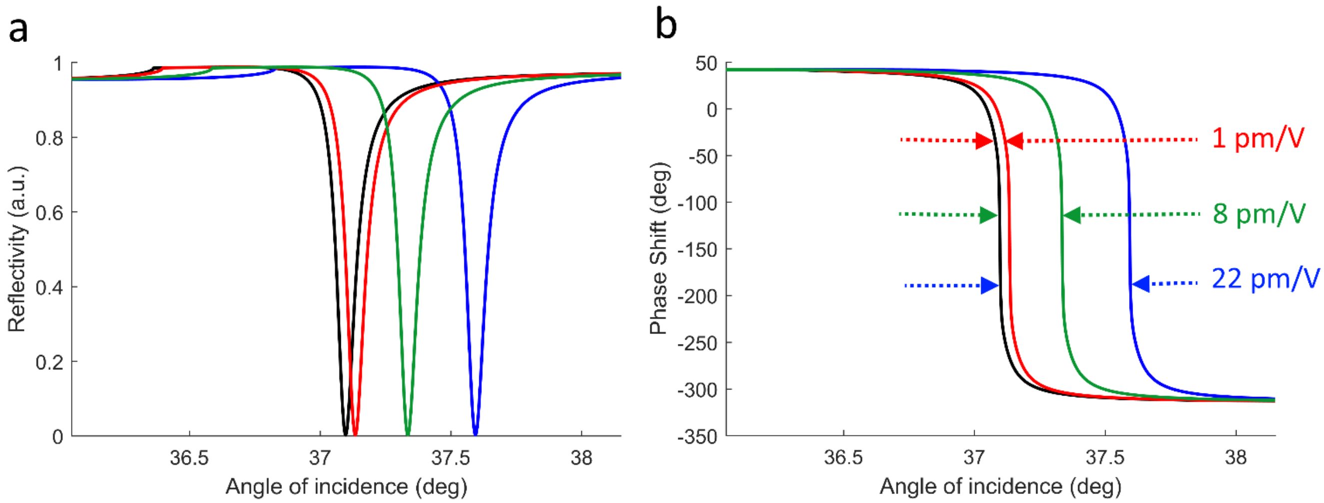

Fig S11. Theoretical reflectivity and phase shifts due to SPR as a function of incident angle for a SI prism with a 48nm Ag SPR film and an EFISH SRN modulation layer (93nm) with an r_{33} coefficient of 1pm/V (red curve), 8pm/V (green curve) and 22 pm/V (blue curve). The black curve represents the angular reflectivity and phase of an unmodulated device. The red curve represents is consistent with the materials used in this work. The blue and green curves represent the phase and intensity of the reflected light as a function of incident angle with the refractive index of an SRN layer shifted via the EFISH effect as reported in [s17] .

References

[1] Dudley, D., Duncan, W.M. and Slaughter, J., 2003, January. Emerging digital micromirror device (DMD) applications. In *MOEMS display and imaging systems* (Vol. **4985,** pp. 14-26). International Society for Optics and Photonics.

[2] Henderson, C.J., Leyva, D.G. and Wilkinson, T.D., 2006. Free space adaptive optical interconnect at 1.25 Gb/s, with beam steering using a ferroelectric liquid-crystal SLM. *Journal of lightwave technology*, ***24*****(5)**, p.1989.

[3] Shrauger, V.; Warde, C. Development of a high-speed high-fillfactor phase-only spatial light modulator. *Proc. SPIE* 2001, 101−108.

[4] Yang, W.; Sun, T.; Rao, Y.; Megens, M.; Chan, T.; Yoo, B.-W.; Horsley, D. A.; Wu, M. C.; Chang-Hasnain, C. J. High speed optical phased array using high contrast grating all-pass filters. *Opt. Express* 2014, **22,** 20038−20044.

[5] Sun, T., Kim, J., Yuk, J.M., Zettl, A., Wang, F. and Chang-Hasnain, C., 2016. Surface-normal electro-optic spatial light modulator using graphene integrated on a high-contrast grating resonator. *Optics express*, **24(23),** pp.26035-26043.

[6] Yu, N., Columbia University of New York, 2015. System, method and computer-accessible medium for depth of field imaging for three-dimensional sensing utilizing a spatial light modulator microscope arrangement. U.S. Patent Application 14/763,925.

[7] Ahearn, J.S., Weiler, M.H., Adams, S.B., McElwain, T.P., Stark, A., DePaulis, L., Sarafinas, A.L., Hongsmatip, T., Martin, R.J. and Lane, B., 2001, November. Multiple quantum well (MQW) spatial light modulators (SLMs) for optical data processing and beam steering. In *Spatial Light Modulators: Technology and Applications* (Vol. **4457,** pp. 43-54). International Society for Optics and Photonics.

[8] Lucente, M., 2011, June. The first 20 years of holographic video—and the next 20. In SMPTE 2nd Annual International Conference on Stereoscopic 3D for Media and Entertainment (pp. 21-23).

[9] Haffner, C., Heni, W., Fedoryshyn, Y., Niegemann, J., Melikyan, A., Elder, D.L., Baeuerle, B., Salamin, Y., Josten, A., Koch, U. and Hoessbacher, C., 2015. All-plasmonic Mach–Zehnder modulator enabling optical high-speed communication at the microscale. *Nature Photonics*, ***9*****(8),** p.525.

[10] Hössbacher, C., Josten, A., Bäuerle, B., Fedoryshyn, Y., Hettrich, H., Salamin, Y., Heni, W., Haffner, C., Kaiser, C., Schmid, R. and Elder, D.L., 2017. Plasmonic modulator with> 170 GHz bandwidth demonstrated at 100 GBd NRZ. *Optics Express*, ***25*(3),** pp.1762-1768.

[11] Zayats, A.V., Smolyaninov, I.I. and Maradudin, A.A., 2005. Nano-optics of surface plasmon polaritons. *Physics reports*, ***408*(3-4),** pp.131-314.

[12] K. Tetz, R. Rokitski, M. Nezhad, and Y. Fainman, “Excitation and direct imaging of surface plasmon polariton modes in a two-dimensional grating”, *Appl. Phys. Lett*. Vol. **86,** No.11, pp. 111110, 2005.

[13] R. Rokitski, KA. Tetz, and Y. Fainman, “Propagation of femtosecond surface plasmon polariton pulses on the surface of a nanostructured metallic film: Space-time complex amplitude characterization,” *Physical Review Letters*, Vol. **95,** No.17, pp.177401-1-177401-4, 21 Oct. 2005.

[14] Huang, Y.H., Ho, H.P., Wu, S.Y. and Kong, S.K., 2012. Detecting phase shifts in surface plasmon resonance: a review. *Advances in Optical Technologies*, *2012*.

[15] Nakkach, M., Duval, A., Ea-Kim, B., Moreau, J. and Canva, M., 2010. Angulo-spectral surface plasmon resonance imaging of nanofabricated grating surfaces. *Optics letters*, ***35*(13),** pp.2209-2211.

[16] Nikitin, P.I., Grigorenko, A.N., Beloglazov, A.A., Valeiko, M.V., Savchuk, A.I., Savchuk, O.A., Steiner, G., Kuhne, C., Huebner, A. and Salzer, R., 2000. Surface plasmon resonance interferometry for micro-array biosensing. *Sensors and Actuators A: Physical*, ***85*(1-3),** pp.189-193.

[17] Dong, W., Pang, K., Luo, Q., Huang, Z., Wang, X. and Tong, L., 2015. Improved polarization contrast method for surface plasmon resonance imaging sensors by inert background gold film extinction. *Optics Communications*, ***346*,** pp.1-9.

[18] Piliarik, M., Vaisocherová, H. and Homola, J., 2005. A new surface plasmon resonance sensor for high-throughput screening applications. *Biosensors and Bioelectronics*, ***20*(10),** pp.2104-2110.

[19] Piliarik, M., Katainen, J. and Homola, J., 2007, May. Novel polarization control for high-throughput surface plasmon resonance sensors. In *Optical Sensing Technology and Applications* (Vol. **6585,** p. 658515). International Society for Optics and Photonics.

[20] Homola, J. and Yee, S.S., 1998. Novel polarization control scheme for spectral surface plasmon resonance sensors. *Sensors and Actuators B: Chemical*, ***51*(1-3),** pp.331-339.

[21] Huang, Y.H., Ho, H.P., Kong, S.K. and Kabashin, A.V., 2012. Phase-sensitive surface plasmon resonance biosensors: methodology, instrumentation and applications. *Annalen Der Physik*, ***524*(11),** pp.637-662.

[22] Moirangthem, R.S., Chang, Y.C., Hsu, S.H. and Wei, P.K., 2010. Surface plasmon resonance ellipsometry based sensor for studying biomolecular interaction. *Biosensors and Bioelectronics*, ***25*(12),** pp.2633-2638.

[23] Liu, C., Liu, Q. and Hu, X., 2014. SPR phase detection for measuring the thickness of thin metal films. *Optics Express*, ***22*(7),** pp.7574-7580.

[24] Yeatman, E.M. and Caldwell, M.E., 1989. Spatial light modulation using surface plasmon resonance. *Applied Physics Letters*, ***55*(7),** pp.613-615.

[25] Kogan, P., Apter, B., Baal-Zedaka, I. and Efron, U., 2008. Resolution improvement of surface plasmon-enhanced, liquid crystal spatial light modulator: Simulation studies. *Optics Communications*, ***281*(18),** pp.4788-4792.

[26] Yariv, A. and Yeh, P., 2006. *Photonics: optical electronics in modern communications*. Oxford Univ..

[27] Xiong, C., Pernice, W.H. and Tang, H.X., 2012. Low-loss, silicon integrated, aluminum nitride photonic circuits and their use for electro-optic signal processing. *Nano letters*, ***12*(7),** pp.3562-3568.

[28] Lin, H.H., Sharma, R., Yang, M.H., Puckett, M.W., Wurm, C.D., Vallini, F. and Fainman, Y., 2017, May. Enhanced effective second-order nonlinearities in Si-rich SiN x thin films. In *Lasers and Electro-Optics (CLEO), 2017 Conference on*(pp. 1-2). IEEE.

[29] Shen, S., Liu, T. and Guo, J., 1998. Optical phase-shift detection of surface plasmon resonance. *Applied optics*, ***37*(10),** pp.1747-1751.

[30] Kurihara, K. and Suzuki, K., 2002. Theoretical understanding of an absorption-based surface plasmon resonance sensor based on Kretchmann's theory. *Analytical chemistry*, ***74*(3),** pp.696-701.

[31] Raether, H., 1988. Surface plasmons on gratings. In *Surface plasmons on smooth and rough surfaces and on gratings* (pp. 91-116). Springer, Berlin, Heidelberg.

[32] Deng, S., Wang, P. and Yu, X., 2017. Phase-Sensitive Surface Plasmon Resonance Sensors: Recent Progress and Future Prospects. *Sensors,* **17(12),** p.2819.

[33] An, Z., Men, C., Xu, Z., Chu, P.K. and Lin, C., 2005. Electrical properties of AlN thin films prepared by ion beam enhanced deposition. *Surface and Coatings Technology*, **196(1-3),** pp.130-134.

[34] Rauthan, C.M.S. and Srivastava, J.K., 1990. Electrical breakdown voltage characteristics of buried silicon nitride layers and their correlation to defects in the nitride layer. *Materials Letters*, **9(7-8),** pp.252-258. (8)

[35] Yota, J., 2011. Effects of deposition method of PECVD silicon nitride as MIM capacitor dielectric for GaAs HBT technology. *ECS Transactions*, **35(4),** pp.229-240.

[36] McManamon, P.F., Bos, P.J., Escuti, M.J., Heikenfeld, J., Serati, S., Xie, H. and Watson, E.A., 2009. A review of phased array steering for narrow-band electrooptical systems. *Proceedings of the IEEE*, 97(6), pp.1078-1096.

[37] Swanson, G.J., 1989. Binary optics technology: the theory and design of multi-level diffractive optical elements (No. TR-854). MASSACHUSETTS INST OF TECH LEXINGTON LINCOLN LAB.

[38] Broomfield, S.E., Neil, M.A.A., Paige, E.G.S. and Yang, G.G., 1992. Programmable binary phase-only optical device based on ferroelectric liquid crystal SLM. *Electronics Letters*, 28(1), pp.26-28.

[39] Weigel, P.O., Savanier, M., DeRose, C.T., Pomerene, A.T., Starbuck, A.L., Lentine, A.L., Stenger, V. and Mookherjea, S., 2016. Lightwave circuits in lithium niobate through hybrid waveguides with silicon photonics. *Scientific reports*, **6**, p.22301.

[40] Chang, L., Pfeiffer, M.H., Volet, N., Zervas, M., Peters, J.D., Manganelli, C.L., Stanton, E.J., Li, Y., Kippenberg, T.J. and Bowers, J.E., 2017. Heterogeneous integration of lithium niobate and silicon nitride waveguides for wafer-scale photonic integrated circuits on silicon. *Optics letters*, **42(4)**, pp.803-806.

[41] Heck, M.J., 2017. Highly integrated optical phased arrays: photonic integrated circuits for optical beam shaping and beam steering. *Nanophotonics*, 6(1), pp.93-107.

[s1]Kolomenski, A., Kolomenskii, A., Noel, J., Peng, S. and Schuessler, H., 2009. Propagation length of surface plasmons in a metal film with roughness. Applied optics, 48(30), pp.5683-5691.

[s2] Smolyaninov, I.I., Mazzoni, D.L. and Davis, C.C., 1996. Imaging of surface plasmon scattering by lithographically created individual surface defects. Physical review letters, 77(18), p.3877.

[s3] M. A. G. Porcel, , J. Mak, C. Taballione, V. K. Schermerhorn, J. P. Epping, P. J. M. V. D. Slot, and K. J. Boller, Optics express 25, no. 26 (2017): 33143-33159.

[s4] Billat, A., Grassani, D., Pfeiffer, M.H., Kharitonov, S., Kippenberg, T.J. and Brès, C.S., 2017. Large second harmonic generation enhancement in Si 3 N 4 waveguides by all-optically induced quasi-phase-matching. Nature communications, 8(1), p.1016.

[s5] Hung-Hsi Lin, Rajat Sharma, Alex Friedman, Benjamin M. Cromey, Felipe Vallini, Matthew W. Puckett, Khanh Kieu, Yeshaiahu Fainman. On observation of dispersion in tunable second-order nonlinearities of silicon-rich nitride thin films. Submitted on 22 Aug 2018. arXiv:1808.07587

[s6] Vlasukova, L.A., Komarov, F.F., Parkhomenko, I.N., Milchanin, O.V., Leont'ev, A.V., Mudryi, A.V. and Togambaeva, A.K., 2013. Optical properties of silicon nitride films formed by plasma-chemical vapor deposition. Journal of Applied Spectroscopy, 80(1), pp.89-92.

[s7] Fletcher, M., Tait, S., Steinlechner, J., Martin, I.W., Bell, A.S., Hough, J., Rowan, S. and Schnabel, R., 2018. Effect of Stress and Temperature on the Optical Properties of Silicon Nitride Membranes at 1,550 nm. Frontiers in Materials, 5, p.1.

[s8] Duquenne, C., Besland, M.P., Tessier, P.Y., Gautron, E., Scudeller, Y. and Averty, D., 2011. Thermal conductivity of aluminium nitride thin films prepared by reactive magnetron sputtering. Journal of Physics D: Applied Physics, 45(1), p.015301.

[s9] Forouzmand, A. and Mosallaei, H., 2016. Tunable two dimensional optical beam steering with reconfigurable indium tin oxide plasmonic reflectarray metasurface. Journal of Optics, 18(12), p.125003.

[s10] McManamon, P.F., Bos, P.J., Escuti, M.J., Heikenfeld, J., Serati, S., Xie, H. and Watson, E.A., 2009. A review of phased array steering for narrow-band electrooptical systems. Proceedings of the IEEE, 97(6), pp.1078-1096.

[s11] Pancharatnam, S., 1955, April. Achromatic combinations of birefringent plates. In Proceedings of the Indian Academy of Sciences-Section A (Vol. 41, No. 4, pp. 137-144). Springer India.

[s12] Victor Bright, David Burns, Steven Gustafson, and Edward Watson. Optical beam steering using surface micromachined gratings and optical phased arrays. Proc. of SPIE, 3131:99,1997.

[s13] David Corkum, Terry Dorschner, Larry Friedman, Douglas Hobbs, Michael Holz, Sergey Liberman, Paul McManamon, Huy Nguyen, Daniel Resler, Richard Sharp, and Edward Watson. Optical phased array technology. Proceedings of the IEEE, 84(2):268, 1996.

[s14] Frankel, M.Y., Matthews, P.J., Esman, R.D. and Goldberg, L., 1998. Practical optical beamforming networks. Optical and quantum electronics, 30(11-12), pp.1033-1050.

[s15] Hans Tholl. Novel laser beam steering techniques. Proc. of SPIE, 6397:639708, 2006.

[s16] Puiu, M. and Bala, C., 2016. SPR and SPR imaging: Recent trends in developing nanodevices for detection and real-time monitoring of biomolecular events. Sensors, 16(6), p.870.

[s17] Hung-Hsi Lin, Rajat Sharma, Alex Friedman, Benjamin M. Cromey, Felipe Vallini, Matthew W. Puckett, Khanh Kieu, Yeshaiahu Fainman. On observation of dispersion in tunable second-order nonlinearities of silicon-rich nitride thin films. Submitted on 22 Aug 2018. arXiv:1808.07587

[s18] Weigel, P.O., Zhao, J., Fang, K., Al-Rubaye, H., Trotter, D., Hood, D., Mudrick, J., Dallo, C., Pomerene, A.T., Starbuck, A.L. and DeRose, C.T., 2018. Hybrid Silicon Photonic-Lithium Niobate Electro-Optic Mach-Zehnder Modulator Beyond 100 GHz. arXiv preprint arXiv:1803.10365.